



HAL
open science

Fe ion-implanted TiO₂ thin film for efficient visible-light photocatalysis

G. Impellizzeri, V. Scuderi, L. Romano, P.M. Sberna, E. Arcadipane, R. Sanz, M. Scuderi, G. Nicotra, Maxime Bayle, Robert Carles, et al.

► **To cite this version:**

G. Impellizzeri, V. Scuderi, L. Romano, P.M. Sberna, E. Arcadipane, et al.. Fe ion-implanted TiO₂ thin film for efficient visible-light photocatalysis. *Journal of Applied Physics*, 2014, 116 (17), pp.173507 - 105308. 10.1063/1.4901208 . hal-01763599

HAL Id: hal-01763599

<https://hal.science/hal-01763599v1>

Submitted on 11 Apr 2018

HAL is a multi-disciplinary open access archive for the deposit and dissemination of scientific research documents, whether they are published or not. The documents may come from teaching and research institutions in France or abroad, or from public or private research centers.

L'archive ouverte pluridisciplinaire **HAL**, est destinée au dépôt et à la diffusion de documents scientifiques de niveau recherche, publiés ou non, émanant des établissements d'enseignement et de recherche français ou étrangers, des laboratoires publics ou privés.

Fe ion-implanted TiO₂ thin film for efficient visible-light photocatalysis

G. Impellizzeri, V. Scuderi, L. Romano, P. M. Sberna, E. Arcadipane, R. Sanz, M. Scuderi, G. Nicotra, M. Bayle, R. Carles, F. Simone, and V. Privitera

Citation: *Journal of Applied Physics* **116**, 173507 (2014); doi: 10.1063/1.4901208

View online: <https://doi.org/10.1063/1.4901208>

View Table of Contents: <http://aip.scitation.org/toc/jap/116/17>

Published by the [American Institute of Physics](#)

Articles you may be interested in

[C ion-implanted TiO₂ thin film for photocatalytic applications](#)

Journal of Applied Physics **117**, 105308 (2015); 10.1063/1.4915111

[Enhanced light scattering in Si nanostructures produced by pulsed laser irradiation](#)

Applied Physics Letters **103**, 221902 (2013); 10.1063/1.4833754

[Superparamagnetism in Co-ion-implanted anatase TiO₂ thin films and effects of postannealing](#)

Applied Physics Letters **83**, 4574 (2003); 10.1063/1.1630841

[Structural defects induced by Fe-ion implantation in TiO₂](#)

Journal of Applied Physics **115**, 053711 (2014); 10.1063/1.4864748

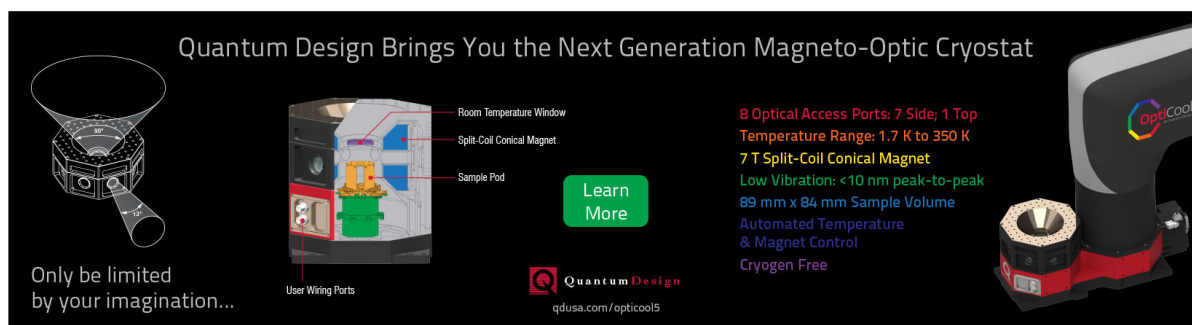
[Electrical and optical properties of TiO₂ anatase thin films](#)

Journal of Applied Physics **75**, 2042 (1994); 10.1063/1.356306

[Ion implantation effects in polycrystalline WO₃ thin films](#)

Journal of Applied Physics **70**, 3509 (1991); 10.1063/1.349244

Quantum Design Brings You the Next Generation Magneto-Optic Cryostat



The advertisement features a central cutaway diagram of the cryostat with labels: Room Temperature Window, Split-Coil Conical Magnet, Sample Pod, and User Wiring Ports. To the left is a 3D perspective view of the device. To the right is a photograph of the physical unit with the 'OptiCool' logo. A 'Learn More' button is positioned in the center.

Only be limited by your imagination...

Learn More

Quantum Design
qdusa.com/opticool5

8 Optical Access Ports: 7 Side; 1 Top
Temperature Range: 1.7 K to 350 K
7 T Split-Coil Conical Magnet
Low Vibration: <10 nm peak-to-peak
89 mm x 84 mm Sample Volume
Automated Temperature & Magnet Control
Cryogen Free

Fe ion-implanted TiO₂ thin film for efficient visible-light photocatalysis

G. Impellizzeri,^{1,a)} V. Scuderi,¹ L. Romano,^{1,2} P. M. Sberna,^{1,2} E. Arcadipane,^{1,2} R. Sanz,¹ M. Scuderi,³ G. Nicotra,³ M. Bayle,⁴ R. Carles,⁴ F. Simone,² and V. Privitera¹

¹CNR-IMM MATIS, Via S. Sofia 64, 95123 Catania, Italy

²Dipartimento di Fisica e Astronomia, Università di Catania, Via S. Sofia 64, 95123 Catania, Italy

³CNR-IMM, Z.I. VIII Strada 5, Catania 95121, Italy

⁴Université de Toulouse, CEMES CNRS, 29 rue Marvig, BP 94347, 31055 Toulouse Cedex 4, France

(Received 23 September 2014; accepted 25 October 2014; published online 6 November 2014)

This work shows the application of metal ion-implantation to realize an efficient second-generation TiO₂ photocatalyst. High fluence Fe⁺ ions were implanted into thin TiO₂ films and subsequently annealed up to 550 °C. The ion-implantation process modified the TiO₂ pure film, locally lowering its band-gap energy from 3.2 eV to 1.6–1.9 eV, making the material sensitive to visible light. The measured optical band-gap of 1.6–1.9 eV was associated with the presence of effective energy levels in the energy band structure of the titanium dioxide, due to implantation-induced defects. An accurate structural characterization was performed by Rutherford backscattering spectrometry, transmission electron microscopy, Raman spectroscopy, X-ray diffraction, and UV/VIS spectroscopy. The synthesized materials revealed a remarkable photocatalytic efficiency in the degradation of organic compounds in water under visible light irradiation, without the help of any thermal treatments. The photocatalytic activity has been correlated with the amount of defects induced by the ion-implantation process, clarifying the operative physical mechanism. These results can be fruitfully applied for environmental applications of TiO₂. © 2014 AIP Publishing LLC.

[<http://dx.doi.org/10.1063/1.4901208>]

I. INTRODUCTION

Since the discovery of the photocatalytic splitting of water on a TiO₂ electrode under ultraviolet (UV) light,¹ semiconductor-based photocatalysis has attracted extensive interest. This work triggered the development of semiconductor photocatalysis for a wide range of environmental and energy applications. In particular, the semiconductor photocatalytic process has shown great potential also in water purification.^{2–4} Titanium dioxide, commonly called *titania*, has proven to be the most promising material due to its many unique properties: non-toxicity, good chemical stability, strong mechanical properties, and low cost. In addition, it is an excellent photocatalyst in the degradation of organic pollutants and in killing microorganisms in water.^{5–10}

The basic principle of photocatalysis can be summarized as follows. Upon absorption of photons with energy equal to or higher than the band-gap of the TiO₂, electrons are excited from the valence band to the conduction band, creating several electron-hole pairs. These charge carriers can migrate to the surface, induce redox reactions in water, and eventually decompose the pollutants adsorbed on the TiO₂ surface into innocuous substances.² Titania exists in two main crystallographic forms: anatase and rutile with band-gaps of 3.15 eV and 3.05 eV, respectively,¹¹ thus requiring UV irradiation in order to be activated.

One of the factors that limit the application of TiO₂ as an efficient photocatalyst is its wide band-gap and the resulting poor absorption of light in the visible (VIS) region. The

development of photocatalysts that can operate under visible light will allow the use of the main part of the solar spectrum and even the poor illumination of interior-lighting. One useful approach has been to dope TiO₂. Asahi *et al.* reported that TiO₂ doping with nitrogen, by sputtering, shifts the optical absorption of the material to the visible range and improves its reactivity for organic molecules under VIS light illumination.¹² One year later, Khan *et al.* chemically synthesized, by flame pyrolysis of a Ti sheet, TiO_{2-x}C_x with a lower band-gap than titania (2.32 versus 3.00 eV).¹³ Doping with transition metals has been also studied.^{3,8,14–16} Metal ion-implantation has been reported as an effective method to improve the visible light response of TiO₂.^{3,17–19} In the ion-implantation process,²⁰ commonly used in the microelectronic industry, the titania is bombarded with metal ions. Although metal ion-implanted TiO₂ (commonly called “second-generation photocatalyst”) is currently believed to be the most effective photocatalyst for solar energy utilization, the operative mechanism together with the photocatalytic performance of the material is not yet clear (see Ref. 3, p. 24). For example, Yamashita *et al.* studied Fe-doped bulk TiO₂ realized by ion-implantation or the sol-gel method.¹⁷ They observed in the case of the chemical doping by sol-gel only a small shift of the absorption band to the visible light regions, in contrast with the larger shift observed for doping with the ion-implantation method. X-ray absorption fine structure analysis suggested that the substitution of Ti atoms in the TiO₂ lattice with implanted metal ions is important in modifying the TiO₂ for the absorption of VIS light.¹⁷ Anpo *et al.* investigated Cr ion-implanted TiO₂ and observed a shift of the absorption band towards the visible light region.¹⁸ They attributed the VIS shift to a modification of

^{a)}Author to whom correspondence should be addressed. Electronic mail: giuliana.impellizzeri@ct.infn.it

the electronic properties of bulk TiO₂ by the implanted metal ions.¹⁸ The authors also excluded a mechanism in which the ion-implanted metals act as electron-hole recombination centers.¹⁸ In addition, to our knowledge, a complete characterization that links UV-VIS absorption, photocatalytic activity, and structural properties of Fe⁺ ion-implanted TiO₂ thin films has not been reported yet.

Thus, the aim of this experimental research was to investigate the effect of Fe⁺ implantation into TiO₂ thin films (~100 nm in thickness) in terms of damage induced by the ion-implantation process into the polycrystalline matrix, optical properties of the synthesised materials, and its photocatalytic activity in the degradation of organic compounds in water under UV or VIS light irradiation. The main objective was to understand the operative physical mechanism and the potential of the system for effective water treatment. Thin films were used in view of the possible applications. Indeed: (1) the use of thin films, instead of bulk materials, is important with the aim of reducing the cost of application; (2) the adequate immobilization of the photocatalyst is relevant in order to suppress expensive filtration or centrifugation processes after the water purification process.

II. EXPERIMENTAL

Titanium layers, ~100 nm thick, were deposited on quartz substrates by sputtering at room temperature. Then, the Ti layers were annealed at 600 °C for 30 min in a conventional furnace under a controlled O₂ flux, in order to induce the complete oxidation of the titanium layer in TiO₂.²¹ The samples were implanted with Fe⁺ ions at 80 keV. The energy was chosen,²² such that the iron implanted profile was fully contained within the TiO₂ layers (Fe projected range ~ 40 nm). The implanted fluences were $2 \times 10^{16} \text{ cm}^{-2}$ (also called through the paper *high fluence*) or $5 \times 10^{15} \text{ cm}^{-2}$ (also called through the paper *low fluence*), so as to produce an iron doping of 5% and 1% by atomic weight. The fluences were fixed as the existing literature suggests that a high concentration of metals is necessary in order to realize a second-generation photocatalyst.^{3,17–19} During implantation, the average current density was ~0.1 μA/cm², and the substrates were held at room temperature. Afterwards, some samples were annealed at 450 or 550 °C for 2 h in an Ar atmosphere, so as to reduce the damage induced by the ion-implantation process.

The composition and the thickness of the films were investigated by Rutherford Backscattering Spectrometry (RBS), with a 3.5 MeV HVEE Singletron accelerator, using a 2 MeV He⁺ beam with 165° scattering angle.

The crystallographic morphology was investigated by transmission electron microscopy (TEM) in a cross sectioned sample, by using a JEOL JEM-2010 F microscope operated at 200 keV.

The structure of the films was studied by Raman scattering with an XploRA Horiba Jobin-Yvon spectrometer using the 532 nm laser line as excitation, and by X-Ray Diffraction (XRD) analyses with a Bruker D-500 diffractometer at several angles of incidence, from 0.8° to 1.0°, and Θ -2 Θ from 20° to 60°. The XRD spectra were analyzed by a Bruker software suite, including the ICSD structure database.

The electrical characterization was carried out by means of a four-point probe, with the samples patterned according to the Van der Pauw geometry (square-shaped 1 cm × 1 cm). The resistivity measurements were affected by a maximum error of about 5%.

The UV-VIS optical characterization was obtained by extracting both the normal transmittance (T) and the 20° reflectance (R) spectra in the 200–800 nm wavelength range, by using a Varian Cary 500 double beam scanning UV/VIS/NIR spectrophotometer.

The photocatalytic activity of the investigated materials was evaluated by the degradation of the methylene blue (MB) organic compound, complying with the ISO protocol.²³ The samples, 0.7 cm × 0.7 cm in size, were immersed in a solution (2 ml) containing MB and de-ionized water (starting concentration: 1.5×10^{-5} M). The mixture was irradiated by an UV lamp (350–400 nm wavelength range) with a power of 8 W, or by a VIS lamp (420–470 nm wavelength range) with a power of 12 W, for a total time of 3 h and a half. A filter able to remove the wavelengths lower than 420 nm was used for the measurements in the visible range. This allowed the contribution of the anatase and rutile band-gaps to be excluded, predicting evidence for the role of the ion-implantation process on the formation of a new effective band-gap. Both the UV and VIS lamps used for the irradiation do not emit in the region of absorption of the MB. As a consequence, the measured degradation of the MB can be only ascribed to the presence of the photocatalysts. Every 30 min of irradiation the solutions were measured with a UV-VIS spectrophotometer (Perkin-Elmer Lambda 35) in a wavelength range between 500 and 800 nm. The degradation of MB was evaluated by the absorbance of the MB peak at 664 nm, according to the Lambert-Beer law ($A = \epsilon \times l \times C$, where A is the absorbance of the solution at 664 nm, ϵ is the extinction molar coefficient, l is the height of the solution, and C is the concentration of the MB).²⁴ The decomposition of the MB in the absence of any photocatalyst materials was also checked as a reference. Before the measurements, the samples were irradiated by the UV lamp for 30 min in order to remove the hydrocarbons localized on the sample surface.²⁵

III. RESULTS AND DISCUSSION

The thickness (~100 nm) and the chemical composition of the TiO₂ films obtained after the oxidation process of the sputtered Ti film were verified by RBS (not shown).

Figure 1 reports the cross-sectional TEM analysis of the TiO₂ sample implanted with the high fluence. Figure 1(a) reports a bright field TEM image showing the quartz substrate covered with a uniform titania layer. The presence of a top most layer of epoxy glue is necessary for cross-sectional TEM sample preparation. Figure 1(b) shows a dark field image of the same region of Fig. 1(a); bright contrast patches highlight both the shape and size of the TiO₂ crystal domains. From the analysis of the dark field images on the TiO₂ film, an average grain size of ~30 nm resulted. The same polycrystalline structure was obtained for the samples implanted with the low fluence, as revealed by the TEM analyses. Therefore, the

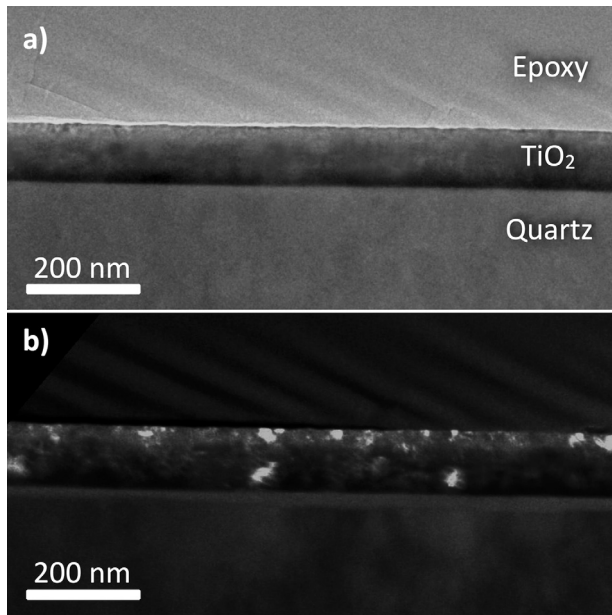


FIG. 1. Cross-sectional TEM images of the TiO₂ film implanted with Fe ($2 \times 10^{16} \text{ cm}^{-2}$ at 80 keV). (a) Bright field image showing a continuous polycrystalline TiO₂ film. (b) Dark field image of the same portion of figure (a); here, the bright contrast regions indicate the presence of different crystal domains due to the polycrystalline nature of the TiO₂ layer.

ion-implantation process was not able to amorphize the titania layer, even in the case of the high fluence.

Figure 2(a) reports (with squares) the RBS spectrum of the TiO₂ film implanted with the Fe ions at a fluence of $2 \times 10^{16} \text{ cm}^{-2}$. The continuous line indicates the simulation of the spectrum obtained by the XRUMP code.²⁶ No change in the relative TiO₂ stoichiometry of the film at the implantation depth was observed, in agreement with the literature data.²⁷ At the projected range of the implanted Fe⁺ ions, the film composition resulted to be Ti 0.9 O 1.8 Fe 0.1, so the relative TiO₂ stoichiometry is maintained even if the concentration of Fe is close to 10% of Ti. Figure 2(b) shows a detail of the Ti and Fe signals in the RBS spectra of the film just

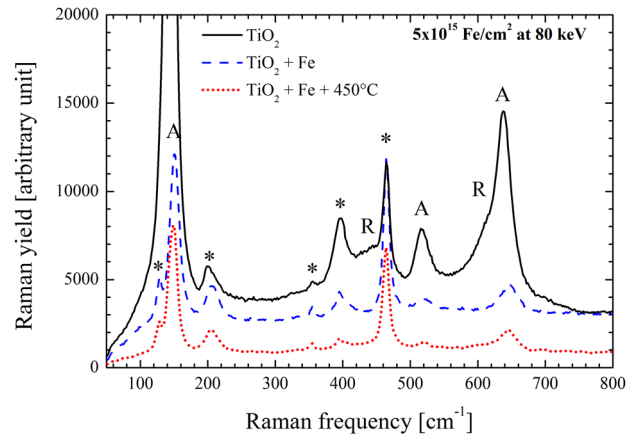
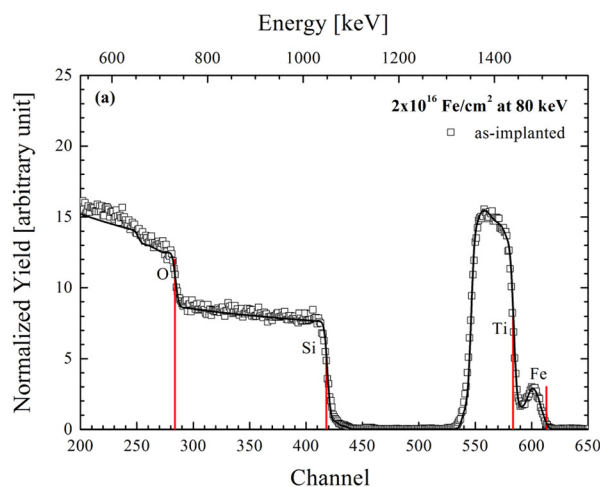


FIG. 3. Raman spectra for the pure TiO₂ film (continuous line), as-implanted with 80 keV Fe at $5 \times 10^{15} \text{ cm}^{-2}$ (dashed line) and after the thermal treatment at 450 °C (dotted line). “A” indicates modes relative to the anatase phase, “R” modes relative to the rutile phase, while “*” indicates modes related to the quartz substrate.

after the ion-implantation and after the thermal process at 550 °C. The Fe atoms clearly diffused during annealing, as indicated by the shift of the iron peak towards the surface. Based on a Gaussian simulation of the Fe profile (lines in Fig. 2(b)) after annealing (XRUMP²⁶) there would appear to be no significant loss of Fe.

The Raman spectra for the TiO₂ film, as-implanted (with the low fluence) and after the thermal treatment at 450 °C, are reported in Fig. 3. The strongest Raman lines at 144, 518, and 638 cm^{-1} can be assigned as E_g, A_{1g}, and E_g modes of the anatase phase,²⁸ respectively (so they are marked by “A” in the figure). We also found two weak peaks near 450 and 610 cm^{-1} that correspond to E_g and A_{1g} modes of the rutile phase,²⁸ respectively (so they are marked by “R” in the figure). The peaks marked by an asterisk come from the quartz substrate, as demonstrated by recording a spectrum from the back side of the samples.

In Fig. 4, a magnification of the Raman spectra is reported (in the frequency range of 500–750 cm^{-1}), for the

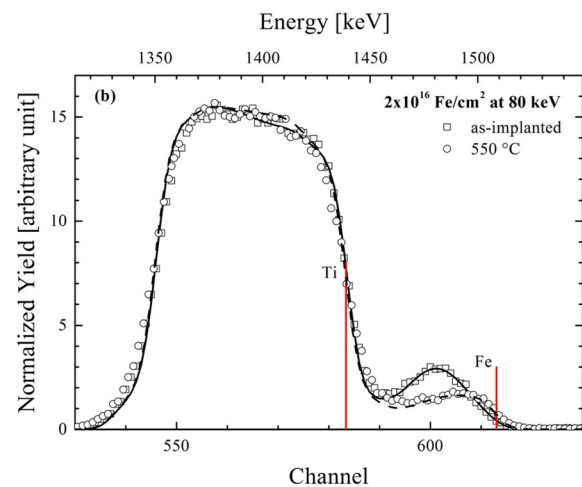


FIG. 2. 2 MeV ⁴He⁺ RBS spectra of TiO₂ films on a quartz substrate implanted with 80 keV Fe at $2 \times 10^{16} \text{ cm}^{-2}$: as implanted sample (a), detail of RBS Ti and Fe signals (b) for the as-implanted (squares) and the annealed at 550 °C (circles) samples. Surface signals of Fe, Ti, O, and Si (from the quartz substrate) are indicated by the vertical red lines. Continuous lines are XRUMP fits to the RBS spectra obtained with a TiO₂ 100 nm thick film and Fe Gaussian implant profiles with a total fluence of $2 \times 10^{16} \text{ cm}^{-2}$.

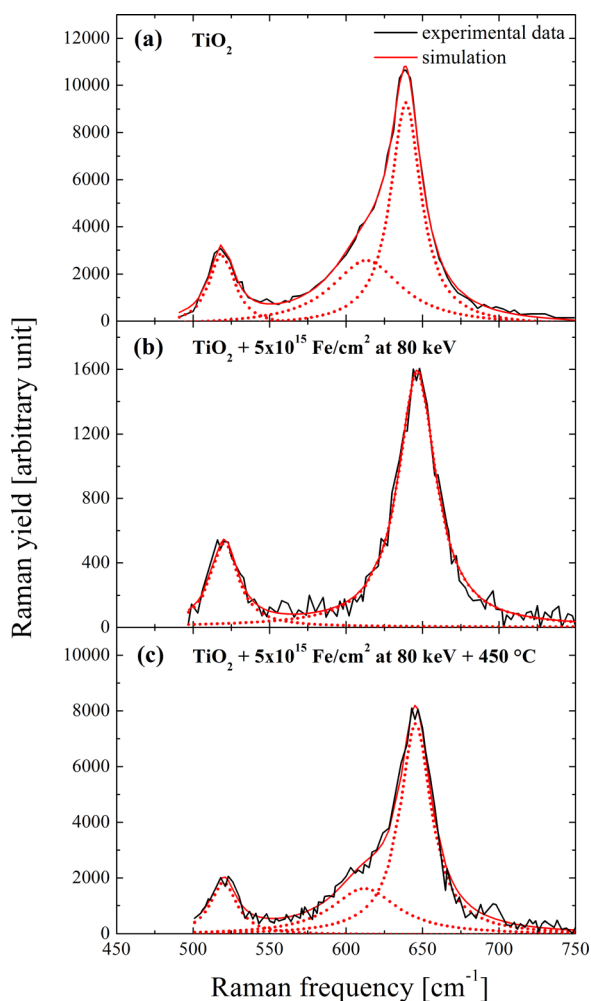


FIG. 4. Magnification of the Raman spectra for the TiO_2 film (a), as-implanted with 80 keV Fe at $5 \times 10^{15} \text{ cm}^{-2}$ (b), and after the thermal treatment at 450 °C (c): data in black continuous lines. In red lines are reported the fit of the spectra with two or three Lorentzian functions.

TiO_2 film (a), as-implanted with 80 keV Fe, $5 \times 10^{15} \text{ cm}^{-2}$ (b), and after the thermal treatment at 450 °C (c). The experimental spectra were fitted by using two or three Lorentzian functions. Before fitting, a monotonous background, mainly due to a highly disordered phase signal, has been extracted. The presence of the rutile mode near 612 cm^{-1} is clearly evidenced in the non-implanted and annealed spectra. The similarity between the spectra of these two samples (namely the same full width at half maximum of the peaks) is consistent with the damage recovery upon annealing. As a matter of fact, the Raman modes are broadened in the non-annealed sample because of the disorder-induced shortening of the phonon correlation length. One notes also that the implantation process induces a blue shift of the highest frequency mode, which is not suppressed by the annealing process. Since disorder effects cannot be invoked here, this may be indicative of the Fe insertion into the TiO_2 matrix, possibly as a result of lattice strain. However, no signature of Fe-O bonding is observed and one may argue that the implantation of Fe^+ ions generates more likely structural defects (vacancies, interstitials, precipitates) than substitutional Fe.²⁹ Despite high levels of damage even after annealing, this conclusion is largely supported by

the channeling RBS data (reported below in Fig. 6), which shows no Fe substitutionality.

The XRD patterns of the starting TiO_2 film, as-implanted and after the thermal treatments are reported in Fig. 5(a) for the iron fluence of $2 \times 10^{16} \text{ cm}^{-2}$, and in Fig. 5(b) for the iron fluence of $5 \times 10^{15} \text{ cm}^{-2}$. The XRD analyses only detected the presence of the anatase and rutile crystalline phases. No peaks related to the Fe_2O_3 or Fe_xTiO_y phases were found in the XRD patterns. Un-implanted films were found to crystallize at 600 °C into anatase and rutile phases. The ion-implantation induced a reduction of the XRD peak intensities, which increases with the fluence. The observed decrease in the intensity can be correlated to a damaging process, typical of ion-implantation.²⁰ The thermal treatments induced, as expected, a damage recovery that was complete for the low fluence but only partially for the high fluence. In addition, the annealing at 550 °C promoted the recovery of the rutile phase.³⁰

In order to improve the investigation of the damage induced by the ion-implantation process on the titania, we performed an Fe^+ implant ($2 \times 10^{16} \text{ cm}^{-2}$ at 80 keV) in a rutile single-crystal (001)-oriented TiO_2 , in order to carry out RBS analyses in the channeling configuration (c-RBS). In Fig. 6, the $\langle 001 \rangle$ channeling spectra of some selected TiO_2 samples are reported. The RBS spectra of the virgin TiO_2 in the random (line plus closed circles) and in channeling configuration (line plus open circles) are shown for a comparison. The as-implanted sample (dotted line) shows a highly damaged region next to the surface. Annealing at 450 and 550 °C produced a change in the lattice damage, as can be

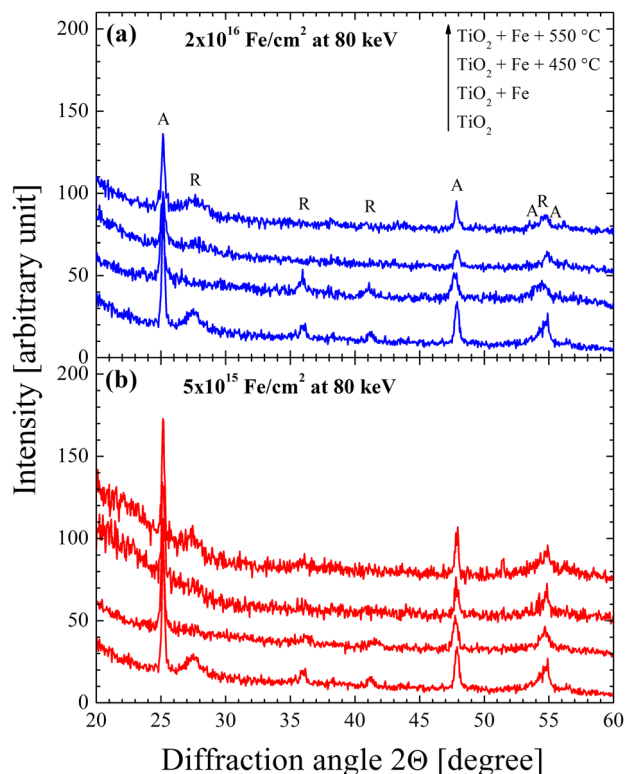


FIG. 5. XRD patterns of the pure TiO_2 film, as-implanted and after the thermal treatments for the Fe^+ fluence of $2 \times 10^{16} \text{ cm}^{-2}$ (a) or $5 \times 10^{15} \text{ cm}^{-2}$ (b) at 80 keV.

inferred by the spectra reported in Fig. 6. By comparing these latter spectra (continuous and dashed lines) with the as-implanted one (dotted line), it can be concluded that the defectiveness induced by the ion implantation with the high fluence was only partially recovered by the thermal treatments. In detail, two defective regions can be clearly distinguished: one peaked at ~ 1430 keV (next to the surface), another one at ~ 1350 keV (deeper in the crystal, probably next to the end-of-range of the implant), neither of them amorphous. These results are in good agreement with the XRD patterns shown in Fig. 5(a). The RBS signals located at ~ 1500 keV are due to the presence of the Fe. In particular, the displacement of the iron peak towards high energy values with annealing is probably due to diffusion/segregation phenomena of the Fe atoms towards the surface, even if no loss of Fe was detected, up to 550°C . Moreover, Fe signal was the same in both random (not shown) and channeling configurations, indicating that Fe atoms are not substitutional in the TiO_2 lattice.

The resistivity of the films implanted with $2 \times 10^{16} \text{ cm}^{-2}$ or $5 \times 10^{15} \text{ cm}^{-2}$ was measured to be 0.4 and $12 \Omega \text{ cm}$, respectively. These values are typical of semiconductor materials. It is worth noting that it was not possible to measure both pure TiO_2 films and the annealed films, because they are excessively resistive. This latter result, along with the decrease of the resistivity with the implanted fluence, can be associated with the defects introduced into the polycrystalline lattice by the ion implantation, which increase the density of the charge carriers.

Figure 7 reports the absorbance for the pure TiO_2 film, an as-implanted sample and a sample after the thermal treatments, for the iron fluence of $2 \times 10^{16} \text{ cm}^{-2}$ (a) or $5 \times 10^{15} \text{ cm}^{-2}$ (b). The absorbance (A) was obtained from the transmittance (T) and reflectance (R) spectra: $A\% = 100 - T\% - R\%$. The reference sample (i.e., the pure TiO_2 film) shows the typical optical absorption in the UV part of the spectrum, for wavelengths shorter than 387 nm (line plus closed circles in Fig. 7). In

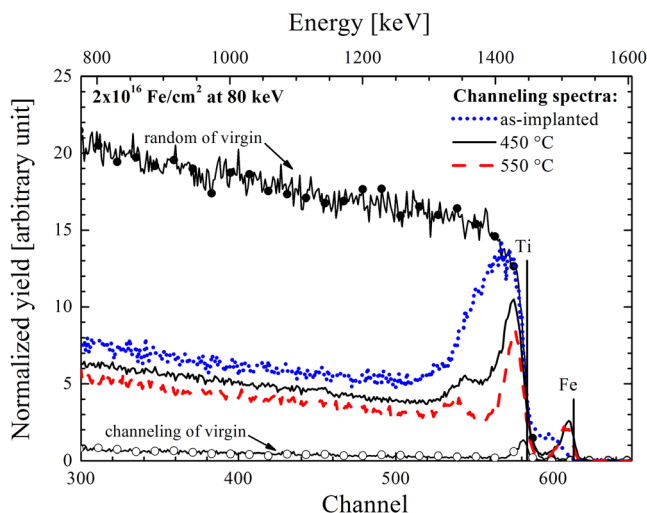


FIG. 6. Channeling RBS spectra for the TiO_2 single crystal after Fe^+ implantation, $2 \times 10^{16} \text{ cm}^{-2}$ at 80 keV (dotted line), and after subsequent annealing at 450°C (continuous line) and at 550°C (dashed line). RBS spectra of a virgin TiO_2 sample in both random (line plus closed circles) and channeling configurations (line plus open circles) are shown for comparison.

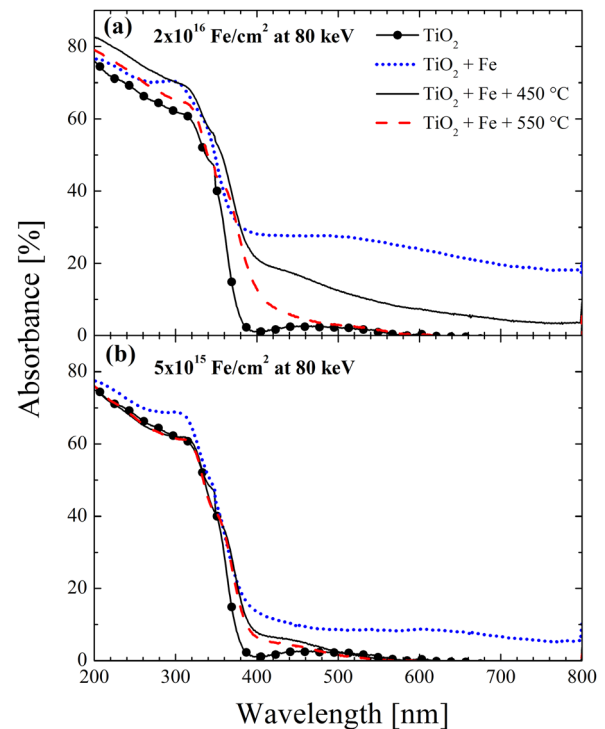


FIG. 7. Absorbance spectra of the pure TiO_2 film, as-implanted and after the thermal treatments for an Fe^+ fluence of $2 \times 10^{16} \text{ cm}^{-2}$ (a) or $5 \times 10^{15} \text{ cm}^{-2}$ (b) at 80 keV .

addition, the iron-implanted films show a remarkable absorption in the VIS part of the spectrum, in the form of a shoulder peak. In detail, the as-implanted samples exhibit an absorbance of $\sim 28\%$ and $\sim 12\%$ for the high and low fluences, respectively, indicating a correlation between the ion fluence and the absorbance of the materials in the VIS. With annealing, the observed trend, for both the fluences, is a decrease of the absorption band in the VIS (see continuous and dashed lines in Fig. 7).

Although doped- TiO_2 has attracted remarkable interest in the recent years, there is not yet a clear explanation for the mechanism responsible for the VIS response (see the Introduction section). The results presented here suggest that ion implantation causes a beneficial damage effect in the TiO_2 film (see the XRD and RBS measurements reported in Figs. 5 and 6, respectively), in good agreement with the literature data (see, for example, Refs. 27 and 29). We suggest that this damage can induce energy levels in the TiO_2 energy band structure, which are responsible for the observed ability of the implanted films to absorb VIS light (see optical measurements reported in Fig. 7). In particular, for higher damage we observe higher VIS absorbance (compare results in Figs. 5 and 6 and Fig. 7). We wish to underline that, differently from the results of Yamashita *et al.*,¹⁷ our study on damage indicates that implanted metal ions do not substitute Ti in the TiO_2 matrix, but occupy interstitial positions in the lattice. In addition, our optical measurements indicate the formation of a new absorption band in the VIS part of the spectrum, which is also different from the shift of the absorption band of the doped titania towards the visible light region observed by Yamashita *et al.* and Anpo *et al.*^{17,18}

Optical spectra were analysed by the Tauc model, which describes the light absorption process in amorphous semi-conductors.³¹ For indirect transitions (that is the case of TiO₂), the Tauc law can be written as follows:³²

$$\alpha = \frac{B}{h\nu} (h\nu - E_g)^2, \quad (1)$$

where B is the Tauc constant,³³ $h\nu$ is the incoming photon energy, E_g is the optical band-gap of the sample, α is the absorption coefficient that is extracted from the transmittance (T) and reflectance (R) measurements performed on each sample by using the following equation:

$$\alpha = \frac{1}{d} \ln \frac{T_Q(1 - R_S)}{T_S}, \quad (2)$$

where d is the thickness of the film, the subscripts Q and S refer to the quartz and the sample, respectively. Another condition of the Tauc law is that α is higher than $1 \times 10^4 \text{ cm}^{-1}$.³¹ Thus, by plotting $(\alpha \times h\nu)^{1/2}$ versus $h\nu$ (the so-called Tauc plot) and fitting with a straight line, E_g can be extracted as its intercept with the abscissa axis. The Tauc plot of the pure TiO₂ film (not shown) gave an energy gap of 3.3 eV. Assuming an error of $\sim 10\%$ in the determination of the band-gap, the value of 3.3 eV is in good agreement with the values reported in the literature for bulk anatase and rutile TiO₂.¹¹ Figure 8 reports the Tauc plot of the TiO₂ film implanted with an iron fluence of $2 \times 10^{16} \text{ cm}^{-2}$ and annealed at 450 °C. The fits (dotted lines in Fig. 8) reveal the presence of two optical band-gaps: one at 3.2 eV, that can be correlated to the titania, and another one at 1.9 eV, which can be correlated to the energy levels introduced in the material by the ion implantation damage. Thus, we locally obtained an effective second band-gap (at 1.9 eV), confined to the most damaged area of the film. It was not possible to apply the Tauc model to the TiO₂ film implanted with the iron fluence of $5 \times 10^{15} \text{ cm}^{-2}$ and annealed at 450 °C, because α is lower than $1 \times 10^4 \text{ cm}^{-1}$.³¹ As a consequence, in order to compare the low and high fluence samples, we estimated the band-gap by simply considering the threshold wavelength in the VIS. The results of this exercise gave a

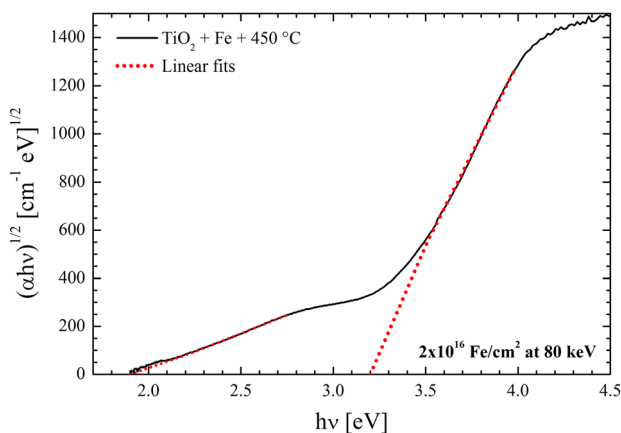


FIG. 8. Tauc plot for the TiO₂ film implanted with Fe⁺ $2 \times 10^{16} \text{ cm}^{-2}$ at 80 keV and annealed at 450 °C (continuous line), together with the linear fit (dotted line).

value of 1.8 eV for the film with the low fluence (1% of iron) and 1.6 eV for the film with the high fluence (5% of iron), both annealed at 450 °C. Given the errors associated with the estimation method this latter value is consistent with the value of 1.9 eV determined above by the Tauc law. It is worth to note that these experimentally obtained effective energy gap values are among the lowest ever reported in the literature.

In order to check the photocatalytic activity of the implanted films in the degradation of organic compounds under UV and VIS irradiation, we performed MB degradation measurements in water by using two different lamps. According to the Langmuir-Hinshelwood model, the photo-mineralization reaction rate, k , of water contaminants is given by the following reaction:

$$\ln\left(\frac{C}{C_0}\right) = -kt, \quad (3)$$

where C is the concentration of organic species, C_0 is the initial concentration of organic species, and t is the time.² We report in Fig. 9 the mineralization rate of the MB, normalized to the value obtained for the MB decomposition in the absence of any catalyst materials, for the different samples, both under UV and VIS light irradiation. On the abscissa axis, *MB* indicates the MB decomposition in the absence of catalyst that is always 1 due to the normalization done (i.e., k/k_{MB}); *TiO₂* refers to the MB decomposition in the presence of a pure TiO₂ film; *as-implanted* indicates the MB decomposition in the presence of Fe⁺-implanted TiO₂ films; etc. Under UV irradiation (Figs. 9(a) and 9(c)), the better response in terms of photodegradation of MB was displayed by the pure TiO₂ films. The photocatalytic efficiency decreased considerably in the case of iron implanted TiO₂, suggesting that the defects induced by the ion implantation work as electron-hole recombination centers, which is different from what was reported by Anpo *et al.*¹⁸ Under VIS irradiation, the situation reversed. In particular, the samples implanted with the high fluence (Fig. 9(b)) show no photocatalytic activity just after the implantation process, but an improvement of 20% and 30% was obtained with the thermal treatments at 450 and 550 °C. These results can be interpreted as follows: the ion-implantation causes a remarkable optical absorption in the VIS range due to the introduction of defects responsible for the formation of energy levels inside the band-gap of the implanted titania. As a consequence, a significant amount of electron-hole couples are formed due to the VIS light irradiation. On the other hand, these energy levels can behave as active sites for the recombination of electron-hole photo-generated couples, decreasing in this way the photocatalytic performance of the material. Thus, our results suggest that ion implantation with a fluence of $2 \times 10^{16} \text{ cm}^{-2}$ is, on one hand, responsible for the reactivity of the material to the VIS light (see Fig. 7(a)), but, on the other hand, the defects induced by the ion implantation cause strong electron-hole recombination, compromising the photocatalytic activity of the as-implanted films. However, with the reduction of defects by annealing (see Fig. 5(a)), an increased photocatalytic activity is observed with VIS light.

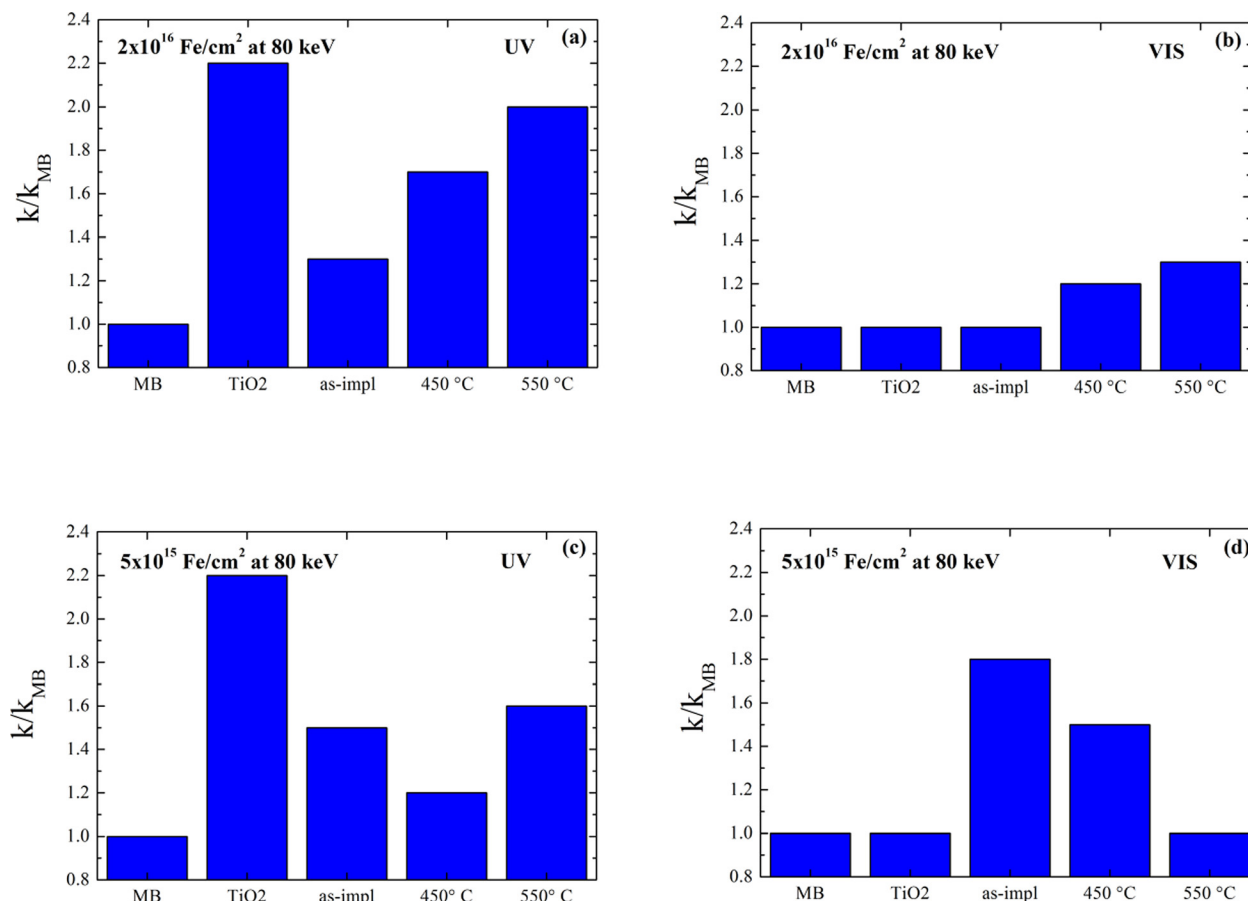


FIG. 9. Photocatalytic rate of MB, normalized to the value obtained for MB in the absence of the photocatalyst, for different Fe^+ implanted films: $2 \times 10^{16} \text{ cm}^{-2}$ (a) and (b), $5 \times 10^{15} \text{ cm}^{-2}$ (c) and (d), both under UV and VIS light irradiation.

The films implanted with the low fluence (Fig. 9(d)) show a more dramatic increase in photocatalytic activity under the VIS irradiation, prior to annealing: an increase of 80% with respect to the pure TiO_2 film. After annealing at 450°C , such an increase is 50%, while it disappears after annealing at 550°C . Following the same reasoning as reported above, the results for the low fluence suggest that the ion implantation introduces defects into the material, which are responsible for VIS light absorption (see Fig. 7(b)), but now the amount of defects is not as high as to negatively affect the efficiency of the mineralization process (through electron-hole recombination). With increasing of the annealing temperature, the efficiency decreases because of the low level of defects: at 550°C , the defect level is low (see Fig. 5(b)) and no energy levels are present inside the band-gap. As a consequence, the implanted films cannot give a photocatalytic response in the VIS (see Fig. 7(b)).

Our experimental results clearly demonstrate that a small effective band-gap (1.6–1.9 eV) can be achieved by Fe^+ irradiation of TiO_2 films, and a marked increase in photocatalytic efficiency can be obtained under VIS light irradiation. Particular attention should be paid to the process, which relies on implantation-induced defects to form energy levels inside the band-gap of the material, but it is crucial to keep their amount below a certain limit, as they act as recombination centres for electrons and holes. We demonstrated that the implantation of a 100 nm thick TiO_2 film with Fe^+ at

$5 \times 10^{15} \text{ cm}^{-2}$, 80 keV induces an absorbance of $\sim 12\%$ for VIS light (see Fig. 7(b)), with an effective band-gap lowering from 3.2 to 1.6–1.9 eV, and a photocatalytic efficiency under the VIS light irradiation that is 80% higher than pure TiO_2 films (see Fig. 9(d)), without the help of any additional thermal treatments.

IV. CONCLUSIONS

In conclusion, we presented a detailed experimental study of the effect of Fe^+ ion-implantation (2×10^{16} or $5 \times 10^{15} \text{ cm}^{-2}$ at 80 keV) on thin TiO_2 pure films (100 nm thick), eventually annealed up to 550°C , so as to realize an efficient second-generation photocatalyst. The reported results confirmed that ion implantation is able to modify TiO_2 pure films, lowering its band-gap energy to around 1.6–1.9 eV, so as to absorb visible light. The measured band-gap was associated with the presence of energy levels inside the energy band structure of the titania, due to implantation-induced defects in the films. The synthesized materials also revealed a marked increase in the photomineralization efficiency under VIS light irradiation (80% higher than the one obtained for pure TiO_2 films), without the help of any additional thermal treatments. We demonstrated that the photocatalytic activity in the degradation of organic compounds strongly depends on the amount of defects induced by the ion-implantation process.

The present research can be considered as an important breakthrough in the utilization of solar light, addressing urgent environmental concerns. In particular, the synthesized materials can be efficiently used for water purification, but can also find applications for the production of hydrogen fuel by water splitting.

ACKNOWLEDGMENTS

The authors wish to thank M. Miritello for fruitful discussion, S. Tatì (CNR-IMM MATIS) and S. Di Franco (CNR-IMM) for their expert technical assistance. This research has been supported by the FP7 European Project WATER (Grant Agreement No. 316082). TEM work was performed at Beyondnano CNR-IMM, supported by the Italian Ministry of Education and Research (MIUR) through the project Beyond-Nano (PON a3_00363).

- ¹A. Fujishima and K. Honda, *Nature* **238**, 37 (1972).
- ²M. N. Chong, B. Jin, C. W. K. Chow, and C. Saint, *Water Res.* **44**, 2997 (2010).
- ³S. Malato, P. Fernández-Ibáñez, M. I. Maldonado, J. Blanco, and W. Gernjak, *Catal. Today* **147**, 1 (2009).
- ⁴M. A. Shannon, P. W. Bohn, M. Elimelech, J. G. Georgiadis, B. J. Marinas, and A. M. Mayes, *Nature* **452**, 301 (2008).
- ⁵D. F. Ollis, *Environ. Sci. Technol.* **19**, 480 (1985).
- ⁶N. Serpone, G. Sauvé, R. Koch, H. Tahiri, P. Pichat, P. Piccinini, E. Pelizzetti, and H. Hidaka, *J. Photochem. Photobiol., A* **94**, 191 (1996).
- ⁷A. Fujishima, T. N. Rao, and D. A. Tryk, *J. Photochem. Photobiol., C* **1**, 1 (2000).
- ⁸X. Chen and S. S. Mao, *Chem. Rev.* **107**, 2891 (2007).
- ⁹V. Scuderi, G. Impellizzeri, L. Romano, M. Scuderi, G. Nicotra, K. Bergum, A. Irrera, B. G. Svensson, and V. Privitera, *Nanoscale Res. Lett.* **9**, 458 (2014).
- ¹⁰V. Scuderi, G. Impellizzeri, L. Romano, M. Scuderi, M. V. Brundo, K. Bergum, M. Zimbone, R. Sanz, M. A. Buccheri, F. Simone, G. Nicotra, B. G. Svensson, M. G. Grimaldi, and V. Privitera, *Nanoscale* **6**, 11189 (2014).
- ¹¹A. Bendavid, P. J. Martin, A. Jamting, and H. Takikawa, *Thin Solid Films* **355**, 6 (1999).
- ¹²R. Asahi, T. Morikawa, T. Ohwaki, K. Aoki, and Y. Taga, *Science* **293**, 269 (2001).
- ¹³S. U. M. Khan, M. Al-Shahry, and W. B. Ingler, Jr., *Science* **297**, 2243 (2002).
- ¹⁴M. I. Litter, *Appl. Catal. B* **23**, 89 (1999).
- ¹⁵S. Zhang, Y. Chen, Y. Yu, H. Wu, S. Wang, B. Zhu, W. Huang, and S. Wu, *J. Nanopart. Res.* **10**, 871 (2008).
- ¹⁶J. Yu, Q. Xiang, and M. Zhou, *Appl. Catal. B* **90**, 595 (2009).
- ¹⁷H. Yamashita, M. Harada, J. Misaka, M. Takeuchi, B. Neppolian, and M. Anpo, *Catal. Today* **84**, 191 (2003).
- ¹⁸M. Anpo and M. Takeuchi, *J. Catal.* **216**, 505 (2003).
- ¹⁹L. Z. Qin, H. Liang, B. Liao, A. D. Liu, X. Y. Wu, and J. Sun, *Nucl. Instrum. Methods Phys. Res., Sect. B* **307**, 385 (2013).
- ²⁰E. Rimini, *Ion Implantation: Basics to Device Fabrication* (Kluwer Academic Publishers, Boston, 1995).
- ²¹D. Veltens, V. Biehl, F. Aubertin, B. Valeske, W. Possart, and J. Breme, *J. Biomed. Mater. Res.* **59**, 18 (2002).
- ²²J. F. Ziegler, J. P. Biersack, and U. Littmark, *The Stopping and Range of Ions in Solids* (Pergamon, New York, 1984), Vol. 1; see <http://www.srim.org> for The Stopping and Range of Ions in Solids.
- ²³H. Zollinger, *Color Chemistry, Synthesis, Properties and Applications of Organic Dyes and Pigments* (VCH, Weinheim, Germany, 1991).
- ²⁴A. D. McNaught and A. Wilkinson, *Compendium of Chemical Terminology, The "Gold Book,"* 2nd ed. (Blackwell Scientific Publications, Oxford, 1997).
- ²⁵R. Wang, K. Hashimoto, A. Fujishima, M. Chikuni, E. Kojima, A. Kitamura, M. Shimohigoshi, and T. Watanabe, *Nature* **388**, 431 (1997).
- ²⁶M. Thompson, see <http://www.genplot.com> for RUMP: Rutherford back-scattering spectroscopy analysis package.
- ²⁷J. Jensen, R. Sanz, D. Martin, A. Surpi, T. Kubart, M. Vázquez, and M. Hernandez-Velez, *Nucl. Instrum. Methods Phys. Res., Sect. B* **267**, 2725 (2009).
- ²⁸W. F. Zhang, Y. L. He, M. S. Zhang, Z. Yin, and Q. Chen, *J. Phys. D: Appl. Phys.* **33**, 912 (2000).
- ²⁹B. Leedahl, D. A. Zatsepin, D. W. Boukhvalov, R. J. Green, J. A. McLeod, S. S. Kim, E. Z. Kurmaev, I. S. Zhidkov, N. V. Gavrilov, S. O. Cholakh, and A. Moewes, *J. Appl. Phys.* **115**, 053711 (2014).
- ³⁰D. A. H. Hanaor and C. C. Sorrell, *J. Mater. Sci.* **46**, 855 (2011).
- ³¹J. Tauc, *Amorphous and Liquid Semiconductors* (Plenum, New York, 1974), p. 175.
- ³²J. Pascual, J. Camassel, and H. Mathieu, *Phys. Rev. Lett.* **39**, 1490 (1977).
- ³³S. Knief and W. von Niessen, *Phys. Rev. B* **59**, 12940 (1999).